Synthesis and characterization of solvated lanthanide(II) bis(triisopropylsilyl)phosphide complexes

Jack Baldwin, Adam Brookfield, George F. S. Whitehead, Louise S. Natrajan,* Eric J. L. McInnes,* Meagan S. Oakley,* David P. Mills*

Department of Chemistry, The University of Manchester, Oxford Road, Manchester, M13 9PL, UK.

*E-mail: david.mills@manchester.ac.uk

Abstract

Lanthanide (Ln) silylamide chemistry is well-developed, but the corresponding silylphosphide chemistry is immature; there are only ten structurally characterized examples of Ln(II) bis(trimethylsilyl)phosphide complexes to date, and no reported derivatives with bulkier R-groups. Here we report the synthesis of the first f-block bis(triisopropylsilyl)phosphide complexes, $[Ln\{P(Si^{i}Pr_3)_2\}_2(THF)_x]$ (**1-Ln**; Ln = Sm, Eu, x = 3; Ln = Yb, x = 2), by the respective salt metathesis reactions of parent $[LnI_2(THF)_2]$ with 2 eq. of $[Na\{P(Si^{i}Pr_3)_2\}]_n$ in toluene. Complexes **1-Ln** were characterized by a combination of NMR, EPR, ATR-IR, electronic absorption and emission spectroscopies, elemental analysis, SQUID magnetometry and single crystal X-ray diffraction. These data contrast with those obtained for related Ln(II) bis(trimethylsilyl)phosphide complexes due to the bulkier ligands in **1-Ln**, and also with Ln(II) bis(triisopropylsilyl)amide complexes due to a combination of longer Ln–P *vs*. Ln–N bonds and the softer nature of P- *vs*. N-donor ligands.

Introduction

Lanthanide (Ln) compounds have unique magnetic, optical and catalytic properties, which have been exploited in a wide range of technological applications.[1] Ln bonding regimes are predominantly ionic and therefore lack directionality, but Ln coordination spheres can be controlled by using appropriate ligands and anaerobic environments.[2,3] Design criteria for Ln complexes with ideal structural features for enhanced physiochemical properties have been developed.[4–9] However, due to Ln ions being hard Lewis acids and their preferential binding to hard Lewis bases such as nitrogen, oxygen and halides, there is a paucity of Ln complexes containing softer p-block donor atom ligands.[1] This is exemplified by the pnictogen series, where there are a large number of structurally authenticated examples of Ln amide complexes,[10–13] but there are few heavy group 15 analogues in comparison.[14–16]

Over the past half a century, bis(trimethylsilyl)amide, $\{N(SiMe_3)_2\}$ (N″), has provided some of the most fascinating advances in Ln chemistry since the first reports of the landmark trigonal pyramidal Ln(III) complexes $[Ln\{N(SiMe_3)_2\}_3]$.[10,17,18] Seminal examples of Ln(II) N″ complexes include the first structurally characterized Eu(II) amide complexes $[Eu\{N(SiMe_3)_2\}_2(sol)_2]$ (sol = DME or THF)[19] and a rare Sc(II) complex $[K(2.2.2\text{-cryptand})][Sc\{N(SiMe_3)_2\}_3]$.[20] Although not as well-established, the larger bis(triisopropylsilyl)amide ligand, $\{N(Si^iPr_3)_2\}$, has also provided notable Ln(II) complexes, such as the near-linear examples $[Ln\{N(Si^iPr_3)_2\}_2]$ (Ln = Sm, Eu, Tm, Yb).[21,22] In contrast, only a handful of f-element bis(trimethylsilyl)phosphide ($\{P(SiMe_3)_2\}$, P″) complexes have been structurally authenticated to date,[14,23,24] and the only Ln(II) examples are $[Sm\{P(SiMe_3)_2\}\{\mu\text{-}P(SiMe_3)_2\}_3Sm(THF)_3]$,[25] $[\{Ln[P(SiMe_3)_2]_3(THF)\}_2(\mu\text{-}I)K_3(THF)]$ (Ln = Sm, Eu), $[KYb\{P(SiMe_3)_2\}_3\{\mu\text{-}K[P(SiMe_3)_2]\}_2]_\infty$, *trans*-$[Ln\{P(SiMe_3)_2\}_2(py)_4]$ (Ln = Sm, Eu, Yb; py = pyridine) and $[Ln\{P(SiMe_3)_2\}_2(18\text{-crown-6})]$ (Ln = Sm, Eu, Yb).[24]

Conversely, to date there are no reported examples of f-element complexes containing bis(triisopropylsilyl)phosphide, $\{P(Si^{i}Pr_3)_2\}$. Whilst $H\{N(Si^{i}Pr_3)_2\}$ and its alkali metal salts can be easily synthesized from commercially available reagents starting from NH_3[21] or $NaNH_2$,[26] $HP(Si^{i}Pr_3)_2$ was previously only isolated as a minor byproduct in 13% yield from the salt metathesis reaction of $[Li(PH_2)(DME)]$ with $ClSi^{i}Pr_3$;[27] the THF-solvated lithium salt, $[Li\{\mu\text{-}P(Si^{i}Pr_3)_2\}(THF)]_2$, was prepared by the deprotonation of $HP(Si^{i}Pr_3)_2$ with $^{n}BuLi$ in THF.[28] Further to this, $[Li(PH_2)(DME)]$ was synthesized from highly toxic gaseous PH_3,[29] and a synthetic route from more readily available red phosphorus has not yet been disclosed; this advance has allowed the chemistry of the smaller phosphide P″ to be developed more rapidly (see above), though this still typically involves the large scale synthesis of $P(SiMe_3)_3$ *via* PNa_3, which requires specialist glassware and protocols.[30]

Here we report the synthesis of the first structurally authenticated Ln(II) $\{P(Si^{i}Pr_3)_2\}$ complexes, $[Ln\{P(Si^{i}Pr_3)_2\}_2(THF)_x]$ (**1-Ln**; Ln = Sm, Eu, $x = 3$; Ln = Yb, $x = 2$). These complexes are characterized by a combination of NMR, EPR, ATR-IR, electronic absorption and emission spectroscopies, elemental analysis, SQUID magnetometry and single crystal X-ray diffraction. We find that the data obtained for **1-Ln** complement and contrast with those previously reported for related Ln(II) P″ and $\{N(Si^{i}Pr_3)_2\}$ complexes, due to differences in ligand steric requirements and hard and soft acid and base (HSAB) considerations.

Results and Discussion

Synthesis

By adapting a combination of literature procedures for the synthesis of $P(SiMe_3)_3$ from PNa_3 with 3 eq. $ClSiMe_3$,[30] the salt metathesis reaction of PNa_3 (prepared *in situ* from red phosphorus, sodium metal and naphthalene) with 3 eq. $ClSi^{i}Pr_3$ in DME at reflux for 24 h gave $[Na\{P(Si^{i}Pr_3)_2\}]_n$ as a white powder in 45% crude yield following work-up.[31] A small portion of the solid was recrystallized from a saturated DME solution to give crystals of the solvated adduct, $[Na\{P(Si^iPr_3)_2\}(DME)_2]$. This method represents a convenient entry point to $\{P(Si^iPr_3)_2\}$ coordination chemistry starting from red phosphorus, where previously PH_3 was used as a starting material (see above).[29] The separate salt metathesis reactions of $[LnI_2(THF)_2]$ (Ln = Sm, Eu, Yb) with 2 eq. of $[Na\{P(Si^iPr_3)_2\}]_n$ in toluene heated at 80 °C for 4 days gave complexes **1-Ln** (Ln = Sm, Eu, Yb) in 43-64% yields following recrystallization from pentane solutions containing several drops of THF (Scheme 1).

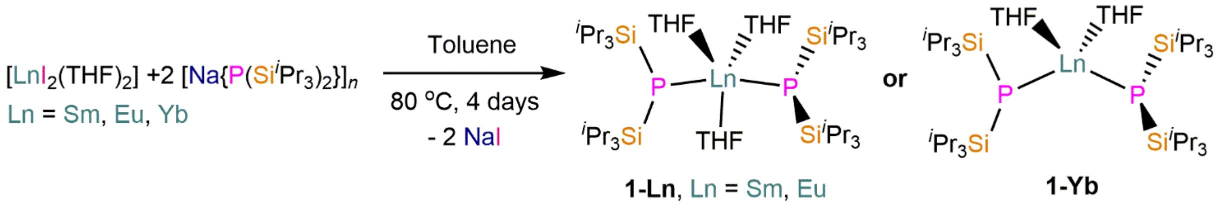

Scheme 1. Synthesis of **1-Ln**.

The bulk compositions of microcrystalline $[Na\{P(Si^iPr_3)_2\}]_n$ and **1-Ln** were assessed by a combination of elemental analysis and ATR-IR spectroscopy (ATR-IR spectra are compiled in the Supporting Information Figures S1-S5). We find that for **1-Ln** elemental analysis results are generally in good agreement with predicted values, but the carbon values obtained were reproducibly lower than expected; we attribute this observation to incomplete combustion arising from carbide formation,[32,33] which is a common feature for analogous Ln $\{N(Si^iPr_3)_2\}$ and Ln $\{P(SiMe_3)_2\}$ complexes.[21,22,34,35]

X-ray Crystallography

The solid state structures of **1-Ln** were determined by single crystal XRD (see Figure 1 for depictions of **1-Eu** and **1-Yb**; $[Na\{P(Si^iPr_3)_2\}(DME)_2]$ is shown in the Supporting Information Figure S6, and as **1-Sm** is isostructural to **1-Eu** it is depicted in Figure S7.

Selected bond distances and angles for all complexes are presented in Table 1, and crystallographic parameters are compiled in Table S1). The Ln(II) ions in the five-coordinate complexes **1-Sm** and **1-Eu** are bound by two $\{P(Si^{i}Pr_3)_2\}$ and three THF ligands in a geometry that is intermediate between trigonal bipyramidal and square-based pyramidal, whilst **1-Yb** has one less THF bound and is distorted tetrahedral (P–Ln–P angles: **1-Sm**: 156.11(3)°, **1-Eu**: 156.10(3)°, **1-Yb**: 133.48(3)°); the lower coordination number in **1-Yb** is due to its smaller size (7-coordinate Ln(II) ionic radii: Sm(II), 1.22 Å; Eu(II), 1.20 Å; Yb(II), 1.08 Å).[6] These geometries were quantified by Shape2.0 (see Supporting Information Tables S3-S4),[37] where the lowest value shape indices of **1-Sm** (3.728) and **1-Eu** (3.718) correspond to a square-based pyramid and that of **1-Yb** (3.311) is a tetrahedron. The distortion of the coordination spheres in five-coordinate complexes can be gauged by the geometric parameter $\tau_5 = (\beta - \alpha)/60$, where β and α are the largest and second-largest angles in the coordination sphere, respectively.[38] The τ_5 parameter quantifies the degree of trigonality within the structural continuum between square-based pyramidal ($\tau_5 = 0$) and trigonal bipyramidal ($\tau_5 = 1$), and the τ_5 values of **1-Sm** (0.8535) and **1-Eu** (0.8560) are closer to the latter (see Supporting Information Table S4). Similarly, four-coordinate systems can be defined by the geometric parameter $\tau_4 = [360 - (\alpha + \beta)]/141$, which quantifies the degree of tetrahedrality between square planar ($\tau_4 = 0$) and tetrahedral ($\tau_4 = 1$).[39] For **1-Yb**, the complex is distorted from an ideal tetrahedral geometry with a τ_4 value of 0.7976 (see Supporting Information Table S4).

The mean Ln–P distances in **1-Ln** (Ln = Sm, 3.0336(13) Å; Eu, 3.024(2) Å; Yb, 2.8065(13) Å) have the expected differences from ionic radii considerations (see above). The Ln–P bond lengths in **1-Ln** are comparable with the respective Ln–P distances seen in $[Sm\{P(SiMe_3)_2\}\{\mu\text{-}P(SiMe_3)_2\}_3Sm(THF)_3]$ (Sm–$P_{terminal}$ = 3.027(3) Å; Sm–$P_{bridging}$ range = 3.100(3)–3.178(3) Å),[23] $[\{Ln[P(SiMe_3)_2]_3(THF)\}_2(\mu\text{-}I)K_3(THF)]$ (Ln = Sm, 2.993(2)–

3.068(2) Å; Eu, 2.988(2)–3.060(2) Å),[24] [Ln{P($SiMe_3$)$_2$}$_2$(18-crown-6)] (Ln = Sm, 3.047(6)–3.126(7) Å; Eu, 3.075(3)–3.099(3) Å),[24] and [Ln{P($SiMe_3$)$_2$}$_2$(py)$_4$] (Ln = Sm, 3.0342(9) Å; Eu, 3.0364(7) Å).[24] However, in **1-Yb** the Yb–P distances are shorter than the Yb–P bonds found in the related Yb(II) phosphide complexes [Yb(PPh_2)$_2$(THF)$_4$] (2.991(2) Å),[40] [Yb{P[CH($SiMe_3$)$_2$](C_6H_3-2-OMe-3-Me)}$_2$(THF)$_2$] (2.969(3) Å),[41] [Yb{P($SiMe_3$)$_2$}$_2$(py)$_4$] (2.9109(10)–2.9358(9) Å), and [Yb{P($SiMe_3$)$_2$}$_2$(18-crown-6)] (2.9662(10) Å).[24] The mean Ln–O distances in **1-Ln** (Ln = Sm, 2.542(3) Å; Eu, 2.527(8) Å; Yb, 2.378(4) Å) all fall within the range of known Ln–O_{THF} bond lengths (2.284(13)–2.951(3) Å for Sm, 2.364(4)–2.811(4) Å for Eu, and 2.167(4)–2.610(3) Å for Yb);[42] those of **1-Sm** are shorter than seen for [Sm{P($SiMe_3$)$_2$}{μ-P($SiMe_3$)$_2$}$_3$Sm(THF)$_3$] (2.593(13) Å mean),[25] and those of **1-Yb** are shorter than observed in both [Yb(PPh_2)$_2$(THF)$_4$] (2.436(5) Å mean)[40] and [Yb{P[CH($SiMe_3$)$_2$](C_6H_3-2-OMe-3-Me)}$_2$(THF)$_2$] (2.534(6) Å mean).[41] We attribute the relatively short Yb–P and Yb–O bond distances in **1-Yb** to the electronically and sterically unsaturated Yb(II) ions, arising from a low metal coordination number.

The geometry of the phosphorus atoms in **1-Ln** are close to ideal trigonal planar, as defined by the sum of the angles about the central phosphorus atom (**1-Sm**, 359.71(8)° and 359.99(8)°; **1-Eu**, 359.72(11)° and 359.99(11)°; **1-Yb**, 358.28(9)° and 359.16(8)°). This differs from the trigonal pyramidal phosphorus geometries in many other Ln(II) bis-phosphide complexes, such as [Sm{P($SiMe_3$)$_2$}{μ-P($SiMe_3$)$_2$}$_3$Sm(THF)$_3$] (326.6(2)°),[25] [Ln{P($SiMe_3$)$_2$}$_2$(py)$_4$] (Ln = Sm, 344.66(9)°; Eu, 344.52(7)°),[24] [Yb(PPh_2)$_2$(THF)$_4$] (332.65(10)°)[40] and [Yb{P[CH($SiMe_3$)$_2$](C_6H_3-2-OMe-3-Me)}$_2$(THF)$_2$] (341.7(7)°).[41] However, there some Ln(II) silylphosphide complexes have exhibited nearly planar phosphorus geometries, such as [Ln{P($SiMe_3$)$_2$}$_2$(18-crown-6)] (Ln = Sm, 352.6(5)° and 354.0(7)°; Eu, 352.1(3)° and 353.9(3)°),[24] [Yb{P($SiMe_3$)$_2$}$_2$(py)$_4$] (359.93(7)°),[24] and [KYb{P($SiMe_3$)$_2$}$_3${μ-K[P($SiMe_3$)$_2$]}$_2$]$_\infty$ (357.5(2) and 358.3(6)°).[24] Although the trigonal planar phosphorus geometries in **1-Ln** could be interpreted as the filled P 3p orbital interacting with the Ln(II) center, this is solely attributed to steric effects due to the electrostatics-dominated bonding regimes in Ln complexes.[1]

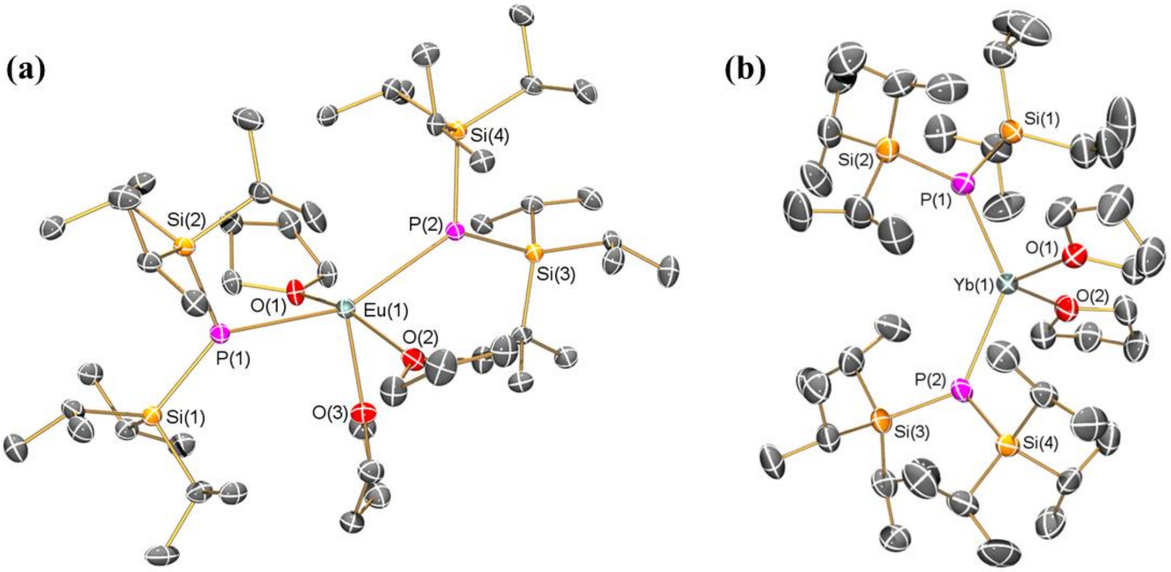

Figure 1. Solid-state structures of (a) **1-Eu**, and (b) **1-Yb**, with selected atomic labeling; Ln = cyan, P = magenta, Si = yellow, O = red, C = gray. Displacement ellipsoids set at 50% probability level, hydrogen atoms omitted for clarity.

Table 1. Selected bond lengths and angles for **1-Ln**.

Parameter	**1-Sm**	**1-Eu**	**1-Yb**
Ln(1)–P(1)/Å	3.0216(10)	3.0107(13)	2.8001(10)
Ln(1)-P(2)/Å	3.0455(8)	3.0366(12)	2.8128(9)
Ln(1)-O(1)/Å	2.553(2)	2.542(4)	2.356(3)
Ln(1)-O(2)/Å	2.556(2)	2.545(4)	2.400(2)
Ln(1)-O(3)/Å	2.516(2)	2.495(4)	-
P(1)–Ln(1)–P(2)/°	156.11(3)	156.10(3)	133.48(3)
O(1)–Ln(1)–O(2)/°	160.08(7)	160.22(12)	99.91(9)
O(1)–Ln(1)–O(3)/°	80.12(7)	80.74(12)	-
O(2)–Ln(1)–O(3)/°	80.56(7)	80.05(12)	-
P(1)–Ln(1)–O(1)/°	93.95(5)	93.66(8)	103.13(8)
P(1)–Ln(1)–O(2)/°	93.81(5)	94.05(9)	103.93(7)
P(1)–Ln(1)–O(3)/°	98.94(6)	99.32(15)	-
P(2)–Ln(1)–O(1)/°	91.73(5)	88.58(8)	96.54(7)
P(2)–Ln(1)–O(2)/°	88.55(5)	91.69(8)	113.68(7)
P(2)–Ln(1)–O(3)/°	104.90(6)	104.52(9)	-
Σ angles about P/°	359.71(8) 359.99(8)	359.72(11) 359.99(11)	358.28(9) 359.16(8)

Solution NMR Spectroscopy

^{1}H, ^{13}C{^{1}H}, ^{29}Si DEPT90 and ^{31}P{^{1}H} NMR spectra were collected for **1-Ln**, and ^{171}Yb{^{1}H} NMR spectra were also obtained for diamagnetic **1-Yb** (see Supporting Information Figures S7-S21 for NMR spectra of all complexes; selected NMR data are compiled in Table 2). Due to the paramagnetism of Sm(II) and Eu(II) ions, significant paramagnetic broadening and shifting of the resonances in the NMR spectra of **1-Sm** and **1-Eu** has reduced the amount of information that can be extracted. In the ^{1}H NMR spectrum of **1-Sm** the methine (δ_H: 1.15 ppm) and methyl (δ_H: 1.29 ppm) resonances of the isopropyl groups were assigned by their relative integrations, but no coupling constants could be determined due to low resolution; two broad resonances at –0.90 and 5.68 ppm were similarly assigned to the α- and β-methylene protons of the three bound THF molecules. In the $^{13}C\{^{1}H\}$ NMR spectrum of **1-Sm** two resonances were also observed for the methine (δ_C: 24.98 ppm) and methyl (δ_C: 28.78 ppm) groups, though the α- and β-positions of THF were not observed due to paramagnetic broadening. No resonances could be confidently assigned to **1-Sm** in the ^{29}Si DEPT90 NMR spectrum, with only a diamagnetic impurity being observed at δ_{Si} = –20.49 ppm; similarly, no resonances corresponding to **1-Sm** were observed in $^{31}P\{^{1}H\}$ NMR spectra collected between +1000 and –1000 ppm, with a singlet at δ_P = –286.50 ppm assigned to a minor impurity of $[Na\{P(Si^{i}Pr_3)_2\}]_n$. The NMR spectra of **1-Eu** exhibit even more pronounced paramagnetic broadening, such that even the ^{1}H NMR spectrum could not be interpreted, though a distinctive resonance was seen at δ_H = 1.26 ppm.

By contrast, all NMR spectra of diamagnetic **1-Yb** could be assigned, though the resonances in the ^{1}H NMR spectra are relatively broad, precluding the extraction of coupling constants. The methyl and methine carbon atoms of the ^{i}Pr groups present as virtual triplets in the $^{13}C\{^{1}H\}$ NMR spectrum of **1-Yb** due to the strongly coupled P atoms, (δ_{Si} = 16.90 ppm, $^{2}J_{PC}$ = 10.3 Hz, ^{i}Pr-*C*H; δ_{Si} = 20.57 ppm, $^{3}J_{PC}$ = 3.6 Hz, ^{i}Pr-*C*H$_3$) whilst a virtual triplet is seen in the ^{29}Si DEPT90 NMR at δ_{Si} = 24.30 ppm ($^{1}J_{PSi}$ = 15.8 Hz) from the same second order effects. The $^{31}P\{^{1}H\}$ NMR spectrum of **1-Yb** exhibits a signal at –301.10 ppm, with satellites to 14.3% abundant $I = ½$ ^{171}Yb nuclei giving $^{1}J_{YbP}$ = 1382 Hz; coupling between the ^{31}P and 4.67% abundant $I = ½$ ^{29}Si nuclei is also observed with $^{1}J_{PSi} \approx 18$ Hz (Figure 2a). This ^{31}P chemical shift value lies downfield to that reported previously for $[Y\{P(SiMe_3)_2\}_2\{\mu\text{-}P(SiMe_3)_2\}]_2$ (δ_P: –104.8 ppm, $^{1}J_{YP}$ = 122.4 Hz; –107.8 ppm, $^{1}J_{YP}$ = 56.7 Hz),[43] and the $^{1}J_{YbP}$ coupling constant is larger than that observed for *trans*-$[Yb(PPh_2)_2(THF)_4]$ (δ_P: –3.0 ppm, $^{1}J_{YbP}$ = 840 Hz),[40] $[Yb\{P(SiMe_3)_2\}_2(py)_4]$ (δ_P: –253.93 ppm, $^{1}J_{YbP}$ = 925 Hz),[24] and $[Yb\{P(SiMe_3)_2\}_2(18\text{-crown-}6)]$ (δ_P: –265.58 ppm, $^{1}J_{YbP}$ = 977 Hz).[24] The $^{171}Yb\{^{1}H\}$ NMR spectrum of **1-Yb** shows the expected triplet resonance at δ_{Yb} = 682 ppm, relative to the

[Yb(Cp*)$_2$(THF)$_2$] (Cp* = C$_5$Me$_5$) external reference, from the respective coupling of ^{171}Yb nuclei with two equivalent 100% abundant I = ½ ^{31}P nuclei (Figure 2b); this is comparable to the doublet of doublets resonance observed for [Yb{P[CH(SiMe$_3$)$_2$](C$_6$H$_3$-2-OMe-3-Me)}$_2$(THF)$_2$] at δ_{Yb} = 663.6 ppm ($^1J_{YbP}$ = 603 and 767 Hz),[42] [Yb{P(SiMe$_3$)$_2$}$_2$(py)$_4$] (δ_{Yb}: 1070 ppm, $^1J_{YbP}$ = 927 Hz),[24] and [Yb{P(SiMe$_3$)$_2$}$_2$(18-crown-6)] ($\delta_{P:}$ 175 ppm, $^1J_{YbP}$ = 977 Hz).[24]

Table 2. ^{1}H, ^{13}C{^{1}H}, ^{29}Si DEPT90, ^{31}P{^{1}H} and ^{171}Yb{^{1}H} NMR data for **1-Sm** and **1-Yb** in C$_6$D$_6$.

Complex	^{1}H (δ)	^{13}C{^{1}H} (δ)	^{29}Si DEPT90 (δ)	^{31}P{^{1}H} (δ)	^{171}Yb{^{1}H} (δ)
1-Sm	–0.90 (br, 12H, THF) 1.15 (br, 12H, ^{i}Pr C*H*) 1.29 (br, 72H, ^{i}Pr CH_3) 5.68 (br, 12H, THF)	24.98 (s, ^{i}Pr *C*H) 28.78 (s, ^{i}Pr *C*H$_3$) THF-C*H*$_2$ not observed	-	-	-
1-Yb	1.41 (br, 92H, ^{i}Pr CH_3, ^{i}Pr C*H* and THF-CH_2) 3.85 (br, 8H, THF-CH_2)	16.90 (Vir. t, ^{i}Pr *C*H, $^2J_{PC}$ = 10.3 Hz) 20.57 (Vir. t, ^{i}Pr *C*H$_3$, $^3J_{PC}$ = 3.6 Hz)	24.30 (Vir. t, P-*Si*, $^1J_{PSi}$ = 15.8 Hz)	–301.10 (s, *P*-Yb, $^1J_{YbP}$ = 1382.1 Hz, $^1J_{PSi}$ = 18.1 Hz)	682 (t, *Yb*-P, $^1J_{YbP}$ = 1382.9 Hz)

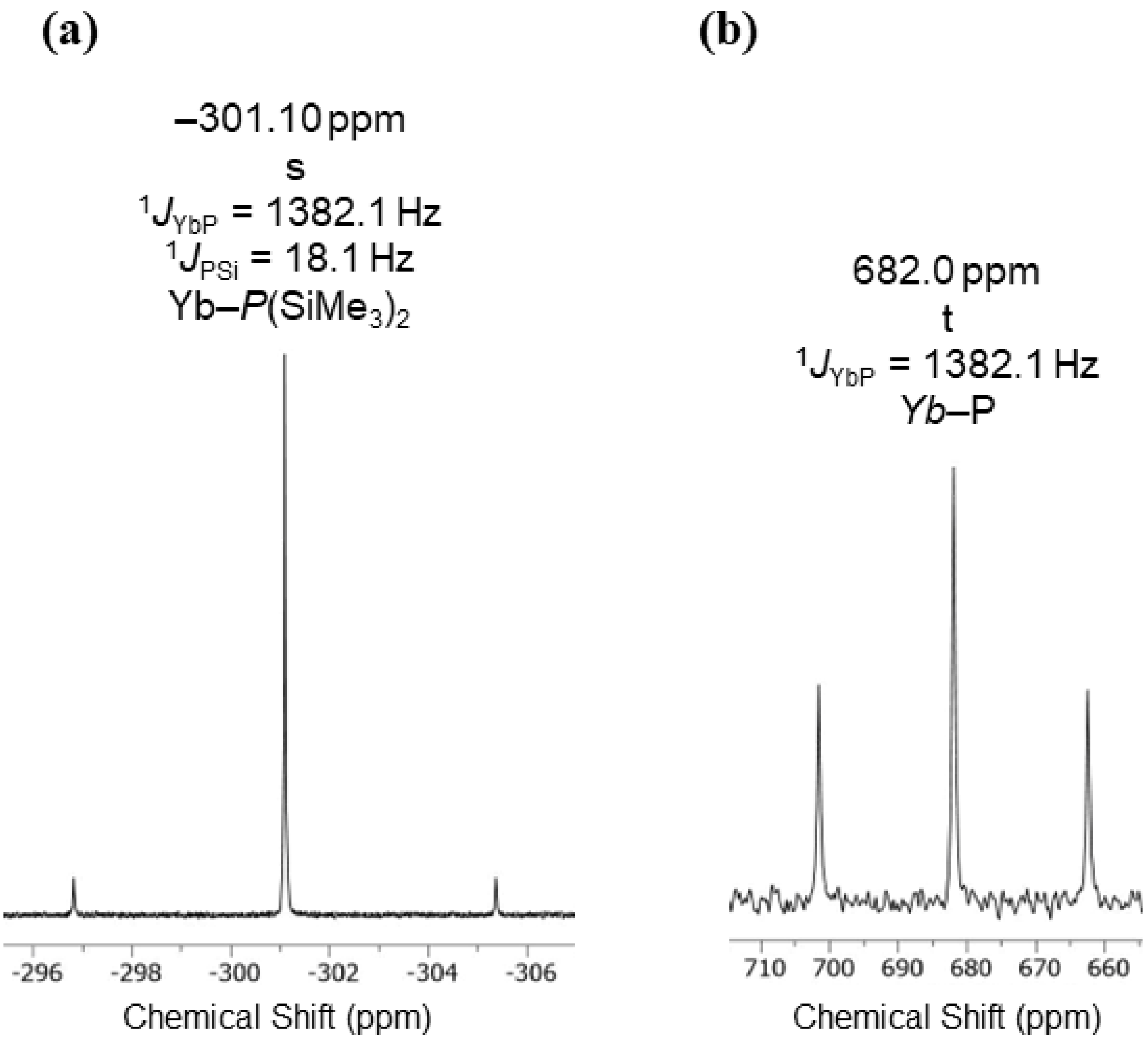

Figure 2. (a) $^{31}P\{^1H\}$ and (b) $^{171}Yb\{^1H\}$ NMR spectra of **1-Yb** in C_6D_6 at 162 MHz and 71 MHz, respectively.

UV-Vis-NIR Spectroscopy

The electronic UV-Vis-NIR absorption spectra of **1-Ln** were recorded as 2 mM toluene solutions (see Figure 3 for compiled spectra; individual spectra are available in the Supporting Information Figures S22-S24). Notably, the absorption bands of Ln(II) complexes are highly sensitive to small changes in the local coordination environment. Strong broad absorptions are often seen in the visible region for Ln(II) complexes due to spin-allowed f-d transitions, where the stabilization of 5d orbitals compared to Ln(III) complexes lower the energy of these Laporte-allowed transitions into the visible region to often mask weaker Laporte-forbidden f-f transitions.[44,45] This is the case for complexes containing Sm(II) ions,[1] and as such toluene solutions of **1-Sm** are deep green, with two broad and intense absorption bands spread across the visible region with λ_{max} = 25,000 cm^{-1} (ε = 776 M^{-1} cm^{-1}) and 17,182 cm^{-1} (ε = 355 M^{-1} cm^{-1}). These absorptions are more intense than the feature in the UV region, which is typically assigned to charge transfer or intra-ligand absorptions.[1] The spectrum of **1-Sm** is comparable with previously reported Sm(II) complexes such as $[Sm\{N(SiMe_3)_2\}_2]_2$ (λ_{max} = 28,600, 24,000, 18,000 and 16,200 cm^{-1})[46] and $[Sm\{N(Si^iPr_3)_2\}_2]$ (λ_{max} = 29,900, 23,500 and 17,200 cm^{-1})[22] as well as for $[\{Sm[P(SiMe_3)_2]_3(THF)\}_2(\mu\text{-}I)K_3(THF)]$ (λ_{max} = 22,730 cm^{-1} (ε = 1575 M^{-1} cm^{-1}), $[Sm\{P(SiMe_3)_2\}_2(py)_4]$ (λ_{max} = 22,525 cm^{-1} (ε = 833 M^{-1} cm^{-1}) and λ_{max} = 13,950 cm^{-1} (ε = 278 M^{-1} cm^{-1}) and $[Sm\{P(SiMe_3)_2\}_2(18\text{-crown-}6)]$ (λ_{max} = 23,150 cm^{-1} (ε = 730 M^{-1} cm^{-1}), λ_{max} = 17,360 cm^{-1} (ε = 488 M^{-1} cm^{-1}) and λ_{max} = 15,385 cm^{-1} (ε = 526 M^{-1} cm^{-1}).[24] By contrast, pale solutions are generally observed for Eu(II) complexes as the Laporte-allowed f-d transitions tend to occur outside the visible region, and the f-f transitions are also spin-forbidden.[1] As such, pale yellow toluene solutions of **1-Eu** are featureless apart from a band that tails into the visible region from the UV. Finally for the Yb(II) complexes no f-f transitions are possible as a result of the 4f^{14} closed shell electronic structure, but the crystal field (CF) imposed can influence colors strongly by varying the energies of the f-d transitions.[1] Toluene solutions of **1-Yb** are pale yellow with a weak band tailing from the UV to the visible region, similar to **1-Eu**, but this band has two distinct shoulders at λ_{max} = 25,641 cm^{-1} (ε = 695 M^{-1} cm^{-1}) and λ_{max} = 23,256 cm^{-1} (ε = 356 M^{-1} cm^{-1}). UV-Vis-NIR absorption spectroscopic data for Yb(II) phosphide complexes are scarce, but $[Yb\{(\mu\text{-}P^tBu_2)_2Li(THF)\}_2]$ possesses absorption features at λ_{max} = 45,000, 37,000, 33,300 and 27,500 cm^{-1},[47] with no bands reported at lower energies whereas [Yb{P(SiMe$_3$)$_2$}$_2$(py)$_4$] has a band at λ_{max} = 17,200 cm^{-1} (ε = 416 M^{-1} cm^{-1}) and [Yb{P(SiMe$_3$)$_2$}$_2$(18-crown-6)] has a band at λ_{max} = 24,750 cm^{-1} (ε = 720 M^{-1} cm^{-1}).[24]

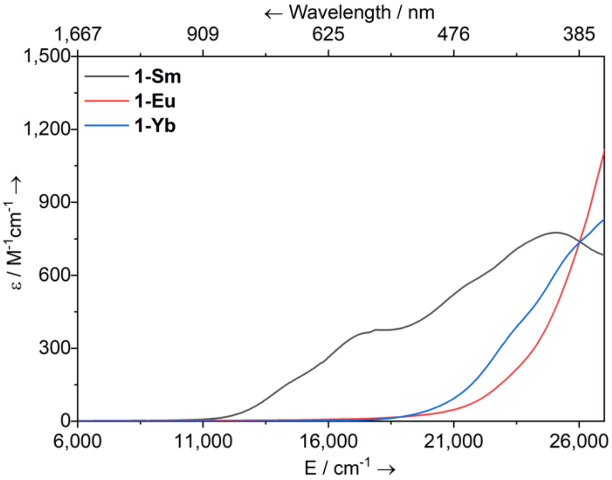

Figure 3. Overlaid electronic UV-Vis-NIR absorption spectra of **1-Ln** (Ln = Sm, Eu and Yb) in toluene (2 mM) between 6,000 – 27,000 cm^{-1} (1667 – 370 nm).

Photoluminescence Studies

We next examined the solution state luminescence properties of **1-Eu** and **1-Yb** at room temperature (Table 3, Figures 4 and Supporting Information Figures S25-S26). Since **1-Sm** possesses intense absorption bands that span the entire visible region, any emission arising from f-d or charge transfer electronic transitions are fully quenched by non-radiative decay mechanisms, hence **1-Sm** is not included in this study. The luminescence of Ln(III) complexes is largely independent of the ligand field, due to the “core-like” nature of the 4f-electrons, and these processes are well-understood.[48] However for Eu(II) and Yb(II), f-d excitations are possible that result in broader, shorter lived visible emission, observable since stabilization of the d-orbitals can change the relaxation pathways that are available to Ln(II) ions.[49,50]

In **1-Eu** and **1-Yb** in fluid toluene solution, excitation between 300 and 410 nm (Figure 4) results in intense vibrationally broadened emission in the green (λ_{em} = 555 nm) and red (λ_{em} = 666 nm) regions of the electromagnetic spectrum, respectively. These emissions are comparable to those reported for [K(2.2.2.cryptand)][Ln{N(Si^{t}BuMe$_2$)$_2$}$_3$],[51] which exhibited emissions within the green (Ln = Eu, λ_{em} = 540 nm) and red (Ln = Yb, λ_{em} = 650 nm) regions, respectively, as well as for the emission reported for [Eu{N(Si^{i}Pr$_3$)$_2$}$_2$] (λ_{em} = 590 nm).[51] These emission wavelengths are comparable to those reported for [{Eu[P(SiMe$_3$)$_2$]$_3$(THF)}$_2$(μ-I)K$_3$(THF)] (λ_{em} = 579 nm), *trans*-[Eu{P(SiMe$_3$)$_2$}$_2$(py)$_4$] (λ_{em} = 579 nm) and [Ln{P(SiMe$_3$)$_2$}$_2$(18-crown-6)] (Ln = Eu, λ_{em} = 475 nm; Yb, λ_{em} = 475 nm).[24] The emission bands in **1-Eu** and **1-Yb** are independent of excitation wavelength in both cases, confirming that the emission originates from a common excited state. The excitation spectrum recorded at the emission maxima for **1-Eu** (Figure 4a) reveals a single, symmetric broad excitation band centered at 340 nm, with no contribution from higher energy charge transfer states. By contrast, the excitation spectrum of **1-Yb** (Figure 4b) possesses two features at 328 and 364 nm, again with no contributions from higher energy electronic excitations. The features in **1-Eu** and **1-Yb** are comparable to those seen for [K(2.2.2.cryptand)][Ln{N(Si^{t}BuMe$_2$)$_2$}$_3$(THF)$_n$] (Ln = Eu, 280 and 330 nm; Yb, 320 and 360 nm).[51] Together, these data indicate that the emission may be a result of deactivation of an f-d excited state that is initially populated by a higher energy charge transfer state.[52]

The luminescence lifetime of **1-Eu** at the emission maxima of 555 nm at room temperature was determined to be monoexponential at 1.42 μs (following excitation with a 375 nm picosecond pulsed diode laser, see Supporting Information Figure S26). This lifetime is slightly shorter than that recorded for [K(2.2.2.cryptand)][Eu{N(Si^{t}BuMe$_2$)$_2$}$_3$] (5.8 ±0.005 μs),[51] but is significantly longer than the luminescence lifetime observed for macrocyclic Eu(II) compounds in solution at room temperature,[53] for example [Eu(benzo-15-crown-5)$_2$][ClO$_4$]$_2$ (0.14 μs in MeOH)[54] and [Eu(benzo-18-crown-6)$_2$][Cl]$_2$ (0.028 μs)[55], and the recently reported phosphide complexes [{Eu[P(SiMe$_3$)$_2$]$_3$(THF)}$_2$(μ-I)K$_3$(THF)] (τ_1 = 811 ns, τ_2 = 1760), *trans*-[Eu{P(SiMe$_3$)$_2$}$_2$(py)$_4$] (τ_1 = 42 ns, τ_2 = 771) and [Ln{P(SiMe$_3$)$_2$}$_2$(18-crown-6)] (Ln = Eu, τ_1 = 447 ns; Yb, τ_1 = 16 ns, τ_2 =

348).[24] However, the lifetime of **1-Eu** is much shorter than for the near-linear Eu(II) complex $[Eu\{N(Si^iPr_3)_2\}_2]$ (49.6 ±1.3 μs).[51] By contrast, the luminescence lifetime of **1-Yb** could not be recorded due to it being shorter than the instrument response function (<0.5 ns), likely as a result of increased competitive non-radiative quenching processes in line with the energy gap law.[56]

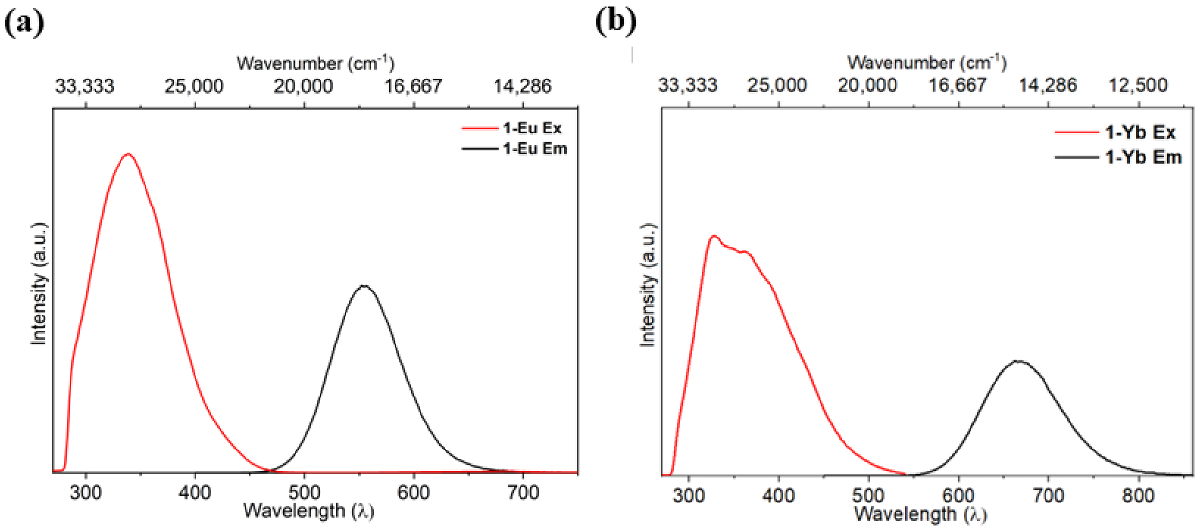

Figure 4. (a) Emission spectrum (**Em**), black trace and excitation spectrum (**Ex**), red trace of complex **1-Eu** in toluene (2.01 mM). Excited at 300 nm (Ex), observed at 555 nm (Em). (b) Emission spectrum (**Em**), black trace and excitation spectrum (**Ex**), red trace of complex **1-Yb** in toluene (0.018 mM). Excited at 300 nm (Ex), observed at 666 nm (Em).

Table 3. Summary of λ_{ex} (nm), λ_{em} (nm) and τ (ns) for complexes **1-Eu** and **1-Yb**.

Complex	λ_{ex} (nm)	λ_{em} (nm)	τ_1 (ns)
1-Eu	375	555	1424
1-Yb	375	666	-

Magnetism

The effective magnetic moment (μ_{eff}) and molar magnetic susceptibility ($\chi_M T$) of powdered samples of paramagnetic **1-Sm** and **1-Eu** suspended in eicosane were examined by variable-temperature DC SQUID magnetometry and Complete Active Space Self-Consistent Field Spin-Orbit (CASSCF-SO) calculations (Selected parameters compiled in Table 4; see Supporting Information Figures S27-S30 for all magnetic data). There is good agreement between measured and calculated magnetization values, and the expected values for the free Eu(II) ion ($4f^7$ $^8S_{7/2}$) for **1-Eu**. However, there is poorer agreement between these values for **1-Sm** (Sm(II) $4f^6$ $^7F_0$) which is likely a consequence of mixing of low-lying ^6F excited states with the magnetic ground state. The saturation magnetization value for **1-Sm** is lower than calculated, which indicates that the ground state is purer than the 80% $m_J = 0$ which is predicted by CASSCF, previously seen in [Sm(Cp^{tt})$_3$] (Cp^{tt} = $C_5H_3{}^tBu_2$-1,3).[57] The absolute values of $\chi_M T$ and magnetization are over-predicted for **1-Eu** by CASSCF however, the shape is accurately reproduced, showing no change in the value of χT upon a decrease in temperature, indicative of a spin-only system.

Table 4. Product of the molar susceptibility and temperature, $\chi_M T$ (cm^3 mol^{-1} K), of **1-Sm** and **1-Eu**, at 2 and 300 K as determined by SQUID magnetometry on powder samples, CASSCF calculations, and free ion values for monomeric ions.

Complex	SQUID Magnetometry		CASSCF Calculations		Free ion[1]
	1.8 K	300 K	2 K	300 K	$\chi_M T$
1-Sm	0.01	1.33	0.31	1.86	1.45
1-Eu	7.30	6.91	7.83	7.86	7.88

EPR Spectroscopy

The electronic structures of the Kramers ion complex **1-Eu** was investigated further by c.w. X-band (*ca*. 9.4 GHz) and Q-band (*ca*. 34 GHz) EPR spectroscopy.

Spectra from the solid state are well-resolved (Figure 5 and S31-S39) with transitions across the entire magnetic field range measured (0 – 1.7 T); those from frozen solution (9 : 1, toluene : hexane, Figures S40-S48) are consistent with the solid-state spectra but are less-well resolved presumably due to strain effects on the structure hence spin Hamiltonian parameters. Hence, we focus our discussion on the solid-state spectra. The spectra were simulated, using EasySpin,[58] with the simple Zeeman and zero-field splitting (ZFS) spin Hamiltonian:

$$\hat{H} = \mu_B g \boldsymbol{B} \cdot \hat{\boldsymbol{S}} + D\left[\hat{S}_z^2 - S(S+1)/3\right] + E\left(\hat{S}_x^2 - \hat{S}_y^2\right)$$

where S is the electron spin quantum number, μ_B is the Bohr magneton, $\boldsymbol{B}$ is the applied magnetic field, g is the electronic g-value (treated as isotropic), and D and E are the axial and rhombic components, respectively, of the ZFS interaction matrix. Higher-order ZFS terms, possible for S = 7/2, were neglected. Good simulations were found with $|D|$ = 4.8 GHz and $|E/D|$ = 0.25 (Figure 5). The high degree of rhombicity (the rhombic limit is given by $|E/D|$ = 1/3) is consistent with the high distortion of the structure of **1-Eu** from trigonal bipyramidal. This rhombicity parameter is larger than we found for the related 6- and 8-coordinate complexes with terminal and *trans*-axial phosphides, $[\mathrm{Ln}\{\mathrm{P(SiMe_3)_2}\}_2(\mathrm{py})_4]$ (D = −3.3 GHz, $|E/D|$ = 0.19) and $[\mathrm{Ln}\{\mathrm{P(SiMe_3)_2}\}_2(18\text{-crown-}6)]$ (D = −5.4 GHz, $|E/D|$ = 0.06), respectively.[24] The magnitude of D for **1-Eu** is intermediate between those two complexes and there does not appear to be an obvious correlation with Eu–P distances or P–Eu–P angles.

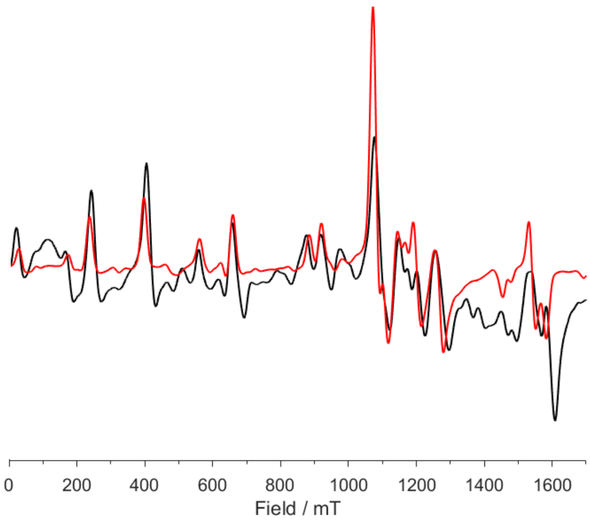

Figure 5. Experimental (black trace) and simulated (red trace) Q-band powder EPR spectra for **1-Eu** at 5 K.

DFT Calculations

The electron density of **1-Yb** was calculated using restricted Kohn-Sham density functional theory with the PBE[59] functional. The Wiberg Bond Order (WBO) and delocalization index, δ(Yb–P), are both used to calculate the number of electrons shared between nuclei of interest. For **1-Yb**, the average between the two Yb–P interactions result in a δ(Yb–P) = 0.25 and a WBO of 0.29. The average value of the electron density at the bond critical point for the Yb–P interactions, ρ_{BCP}(Yb–P), is 0.027 a.u., which confirms that these interactions are weak. This is also corroborated with the highest occupied molecular orbital which has a lack of orbital overlap between metal and ligand (see Supporting Information Figure S51).

Ab initio Calculations

The electronic structures of **1-Sm** and **1-Eu** were investigated by CASSCF-SO calculations using the OpenMolcas package (see Supporting Information Table S6 and S7 and Figures S49 and S50).[60] There is a mixed ground state for **1-Eu** consisting of $|\pm 1/2\rangle$ (41%), $|\pm 3/2\rangle$ (39%), $|\mp 5/2\rangle$

(11%), and $|\pm 1/2\rangle$ (6%) with g_1 = 12.25, g_2 = 2.81, g_3 = 1.24, where the largest g-value is approximately perpendicular with the P–Eu–P axis, suggesting that the intermediate m_J states are stabilized both by the hard O-donor atoms of THF and the two softer silylphosphide ligands. Conversely, **1-Sm** has a reasonably isolated ground state consisting of $|0\rangle$ (80%).

Conclusion

The solvated Ln(II) bis(triisopropylsilyl)phosphide complexes **1-Ln** (Ln = Sm, Eu, Yb) are straightforwardly prepared by salt metathesis methods, and represent the first examples of structurally authenticated f-block complexes containing this bulky phosphide ligand. We find complementary and contrasting behavior of the solid-state structures and spectroscopic data of **1-Ln** to related Ln(II) complexes of the bulky bis(silyl)amide $\{N(Si^iPr_3)_2\}$ and the smaller bis(silyl)phosphide $\{P(SiMe_3)_2\}$, driven by a combination of differing steric effects and ligand hardness. The reactivity of **1-Ln** and related derivatives should be rich due to the tendency of Ln(II) complexes to reduce substrates by single electron transfer,[1] thus their redox chemistry will be investigated in future studies.

Experimental

General. All manipulations were conducted under argon with the strict exclusion of oxygen and water by using Schlenk line and glove box techniques. $[LnI_2(THF)_2]$ (Ln = Sm, Eu, Yb) were prepared following literature procedures,[61] whilst $[Na\{P(Si^iPr_3)_2\}]_n$ was either prepared by the method below or by an improved synthesis.[31] THF, pentanes and toluene were purged with nitrogen and passed through columns containing alumina catalyst and molecular sieves before being degassed, refilled with argon and stored over activated 4 Å molecular sieves (THF) or a potassium mirror (pentanes, toluene) before use. For NMR spectroscopy, d_6-benzene and d_8-THF were dried by refluxing over K, and were vacuum transferred and degassed by three freeze-pump-thaw cycles before use. NMR spectra were recorded on a JEOL JNM-ECZ 400 MHz spectrometer operating at 399.78 (^{1}H), 100.52 (^{13}C{^{1}H}), 79.42 (^{29}Si DEPT90) MHz, referenced to $SiMe_4$, 161.83 (^{31}P{^{1}H}) MHz referenced to 85% H_3PO_4 and 70.67 (^{171}Yb{^{1}H}) MHz, referenced to $[Yb(Cp^*)_2(THF)_2]$. FTIR spectra were recorded on microcrystalline solids using a Bruker Alpha spectrometer with a Platinum-ATR module. UV-Vis-NIR spectroscopy were recorded on a Perkin Elmer Lambda 750 spectrometer on 2 mM toluene solutions in a 1 cm path length cuvette and were corrected to a toluene reference cell. Elemental analysis was carried out by Mr Martin Jennings and Mrs Anne Davies at the Microanalytical service, School of Chemistry, the University of Manchester using a Thermo Scientific Flash Smart Elemental Analyzer with D4001 Flat Base Smooth Wall Tin Capsules (6 × 3 mm). Elemental analysis results for **1-Ln** reproducibly gave low carbon values; this has consistently been seen for $\{N(Si^iPr_3)_2\}$ complexes and we have previously attributed this observation to the formation of carbides from incomplete combustion.[21,22,32–35]

The crystal data for $[Ln\{P(Si^iPr_3)_2\}_2(THF)_x]$ (1-Ln; Ln = Sm, Eu, $x = 3$; Ln = Yb, $x = 2$) and $[Na\{P(Si^iPr_3)_2\}(DME)_2]$ are compiled in Tables S1 and S2. Crystals were examined using a Rigaku XtalLAB AFC11 diffractometer equipped with a CCD area detector and graphite-monochromated Cu Kα (λ = 1.54178 Å) or Mo Kα radiation (λ = 0.71073 Å). Intensities were integrated from data recorded on 1° frames by ω rotation. Cell parameters were refined from the observed positions of all strong reflections in each data set. A Gaussian grid face-indexed correction was used to account for X-ray absorption.[62] The structures were solved using SHELXS.[63] Datasets were refined by full-matrix least-squares on all unique F^2 values,[64] with anisotropic displacement parameters for all non-hydrogen atoms, and with constrained riding hydrogen geometries; Uiso(H) was set at 1.2 (1.5 for methyl groups) times Ueq of the parent atom. The largest features in final difference syntheses were close to heavy atoms and were of no chemical significance. CrysAlisPro[62] was used for control and integration, and SHELX[63,64] was employed through OLEX2[65] for structure solution and refinement. ORTEP-3[66] and POV-Ray[67] were employed for molecular graphics.

Steady state and time resolved emission spectra were recorded at room temperature from 300–800 nm in Youngs tap-appended 10 mm pathlength quartz cuvettes on an Edinburgh Instruments FLS-1000 photoluminescence spectrometer equipped with a 450 W steady state xenon lamp, a 60 W microsecond pulsed xenon flash lamp and interchangeable picosecond pulsed diode lasers (EPL-375 and EPL-405), with single 325 mm focal length excitation and emission monochromators in Czerny Turner configuration and a red sensitive photomultiplier in Peltier (air cooled) 53 housing (Hamamatsu R928P). Lifetime data were recorded following excitation at 375 nm by the EPL-375 diode laser using time correlated single photon counting (TCSPC). Lifetimes were obtained by tail fit on the data obtained. Plotting, fitting and analysis of data were carried out using the in-built instrumental software and Origin 2019b. All data were fitted with exponential decay models and the goodness of fit evaluated by minimization of the residuals squared, χ^2 and R^2 analysis.

Magnetic data were collected on a Quantum Design MPMS3 superconducting quantum interference device (SQUID) magnetometer using doubly recrystallized powdered samples. Samples were prepared in an NMR tube containing finely ground powders of crystalline material (**1-Sm**: 32.3 mg; **1-Eu**: 15.2 mg). Eicosane was added (**1-Sm**: 17.5 mg; **1-Eu**: 7.2 mg) and the samples briefly heated to melt this wax, which then acted as a restraint when the samples were allowed to cool and set; these tubes were then flame-sealed under vacuum to *ca*. 5 cm in length. The ampoules were mounted in plastic straws, held in place with diamagnetic tape. Samples were carefully checked for purity and data reproducibility between several independently prepared batches. Measurements were corrected for the contribution of the blank sample holders (flame-sealed Wilmad NMR tube and straw) and eicosane matrix, corrected for both the shapes of the sample using the MPMS3 Geometry Simulator (correction factors 0.974–1.075) and the diamagnetic contributions, which were approximated as the molecular weights multiplied by 0.5×10^{-6} cm^3 K mol^{-1}. Variable temperature magnetic susceptibility measurements were collected under an applied field (**1-Sm**: 0.1 T, **1-Eu**: 0.1

T) using VSM mode with 5 mm amplitude and 2 s averaging time. Isothermal magnetization measurements were performed in DC scan mode with 40 mm scan length and 6 s scan time.

Continuous Wave (CW) X-band (*ca*. 9.4 GHz) spectra were recorded with a Bruker EMX spectrometer fitted with a Super High Q X-band resonator and at Q-band (*ca*. 33.9 GHz) microwave frequency using a Bruker EMX300 spectrometer. Polycrystalline and frozen solution (9:1 toluene:hexane, 10mM) samples of **1-Eu** were sealed in quartz X-band and Q-band EPR tubes in *vacuo*; samples were lightly ground with a mortar and pestle to reduce the amount of sample decomposition, but we note that some effects due to polycrystallinity remain in the spectra below. The presence of a very sharp resonance at g = 2.00 is attributed to an impurity in the quartz EPR tubes, and serves as an internal reference for comparing relative intensities.

OpenMolcas[60] (version v19.11-d14be45) was used to perform CASSCF-SO calculations on **1-Sm** and **1-Eu** to determine the electronic structure. The molecular geometry from a single crystal XRD structure was used with no optimization, selecting a single molecule from the asymmetric unit and taking the largest disorder component only. Electron integrals were calculated in the SEWARD module using basis sets from the ANO-RCC library[68,69] with VTZP quality on the metal atom, VDZP quality on the P and O atoms and VDZ quality on all other atoms, employing the second-order DKH Hamiltonian to account for scalar relativistic effects. Resolution of identity Cholesky decomposition of the two-electron integrals with on-the-fly auxiliary atomic compact Cholesky decomposition (acCD) basis sets was used to save disk space and to reduce computational demand.[70] The molecular orbitals (MOs) were optimized using state-averaged CASSCF (SA-CASSCF) calculations in the RASSCF module, with a CAS(n,7) calculation where the active space included the valence 4f electrons (n) and the seven 4f orbitals. For **1-Sm**, SA-CASSCF calculations were performed for all possible spins and configuration state functions: 7 heptets. For **1-Eu**, SA-CASSCF calculations were performed for all possible spins and the following number of roots: 1 octet, 48 sextets, 392 quartets, and 560 doublets. A subset of these roots was then mixed by spin orbit coupling in the RASSI module, where 1 octet, 48 sextets, 119 quartets and 113 doublets were included. SINGLE_ANISO was used to decompose the resulting spin-orbit wave functions into the CF Hamiltonian formalism.[71] Diamond was employed for molecular graphics.[72]

Density functional theory was used to optimize the hydrogen positions of **1-Yb**, while all other atoms were kept frozen at the crystal structure positions; this was done using the PBE[59] density functional with the Stuttgart RSC 1997 ECP for Yb[73] and cc-pDVZ[74] basis set for the ligand atoms, and dispersion interactions were included with the D3 dispersion correction.[75,76] All DFT calculations were performed with Gaussian 16 Rev C.01.[76] Multiwfn 3.8[77] was used to perform analysis of the total electron density.

[Na{P(Si^{i}Pr$_3$)$_2$}]. A three neck 500 mL round bottom Schlenk was charged with red phosphorus (3.100 g, 100.0 mmol) and dried under vacuum for *ca*. 12 hours. DME (*ca*. 250 mL) and naphthalene (3.00 g, 23.4 mmol) were added. Chunks of Na washed in hexane (6.897 g, 300.0 mmol, 3 eq.) were added in small portions over the space of 30 mins. The reaction mixture was stirred at reflux (100 °C) for 16 hours, and became dark green in color. A dropping funnel was charged with Si^{i}Pr$_3$Cl (45.0 mL, 2.1 eq.) and this was added dropwise to the reaction mixture at room temperature. The reaction mixture was stirred at reflux (100 °C) overnight, and became purple in color. This was allowed to cool and was filtered into a 3-neck round bottom Schlenk (500 mL) through a fritted Schlenk *via* a wide-bore cannula. The solvent was removed from the resultant yellow-orange solution under vacuum to yield a yellow/orange oily-solid, with crystalline material forming when dried *in vacuo*. The oil was washed with pentane (100 mL), filtered and the remaining off-white solid was dried in *vacuo*. Yield = 5.489 g, 10 mmol, 10%. Crystals of [Na{P(Si^{i}Pr$_3$)$_2$}(DME)$_2$] were obtained by recrystallization of the off-white solid from a saturated DME solution, and this was found to desolvate under vacuum. Anal calcd (%) for $C_{18}H_{42}PSi_2Na$: C, 58.64; H, 11.48. Found (%):

C, 58.29; H, 11.55. ^{1}H NMR (400 MHz, d_8-THF, 298 K): δ 1.02 (m, 6H, C*H*(CH$_3$)$_2$), 1.11 (d, $^{3}J_{\mathrm{HH}}$ = 6.9 Hz, 36H, CH(C*H*$_3$)$_2$). ^{13}C{^{1}H} NMR (101 MHz, d_8-THF, 298 K): δ 17.47 (d, $^{2}J_{\mathrm{PC}}$ = 9.9 Hz, *C*H(CH$_3$)$_2$, 21.18 (d, $^{3}J_{\mathrm{PC}}$ = 3.8 Hz, CH(*C*H$_3$)$_2$). ^{29}Si DEPT90 NMR (79 MHz, d_8-THF, 298 K): δ 20.65 (d, $^{1}J_{\mathrm{PSi}}$ = 59.8 Hz (P*Si*). ^{31}P{^{1}H} NMR (162 MHz, d_8-THF, 298 K): δ –384.26 (s, Na*P*). FTIR ν/cm^{-1}: 2937 (s), 2859 (s), 1461 (m), 1359 (m), 1239 (w), 1015 (m), 1011 (s), 876 (s), 619 (s).

[Sm{P(Si^{i}Pr$_3$)$_2$}$_2$(THF)$_3$] (1-Sm). A suspension of [SmI$_2$(THF)$_2$] (0.5490 g, 1.00 mmol) and [Na{P(Si^{i}Pr$_3$)$_2$}]$_n$ (1.1698 g, 2.00 mmol) in toluene (50 mL) was heated at 80 °C for 4 days to give a green-brown reaction mixture. The volatiles were removed in *vacuo* and the product was extracted with pentanes (20 mL) and filtered. The filtrate was concentrated to *ca*. 5 mL, and a few drops of THF were added before the flask was stored at –30 °C to give dark green crystals of the title complex, which were isolated and dried *in vacuo*. Yield = 0.6817 g, 0.644 mmol, 64%. Anal calcd (%) for $C_{48}H_{108}O_3P_2Si_4Sm$: C, 54.49; H, 10.29. Found (%): C, 52.66; H, 10.49. ^{1}H NMR (400 MHz, d_6-benzene, 298 K): δ –0.90 (br, 12H, THF-C*H*$_2$), 1.15 (br, 12H, C*H*(CH$_3$)$_2$), 1.29 (br, 72H, CH(C*H*$_3$)$_2$), 5.68 (br, 12H, THF-C*H*$_2$). ^{13}C{^{1}H} NMR (101 MHz, d_6-benzene, 298 K): δ 24.98 (*C*H(CH$_3$)$_2$), 28.78 (CH(*C*H$_3$)$_2$), THF signals not observed. ^{29}Si DEPT90 NMR (79 MHz, d_6-benzene, 298 K): No signal observed for **1-Sm** between +250 and -250 ppm due to paramagnetic broadening. ^{31}P{^{1}H} NMR (162 MHz, d_6-benzene, 298 K): No signal observed for **1-Sm** between +1000 and –1000 ppm due to paramagnetic broadening. FTIR ν/cm^{-1}: 2933 (m), 2853 (s), 1461 (m), 1375 (w), 1258 (w), 1071 (w), 1015 (m), 882 (s).

[Eu{P(Si^{i}Pr$_3$)$_2$}$_2$(THF)$_3$] (1-Eu). Prepared by the same method as **1-Sm** using [EuI$_2$(THF)$_2$] (0.4275 g, 0.777 mmol) and [Na{P(Si^{i}Pr$_3$)$_2$}]$_n$ (0.8533 g, 1.555 mmol) to give yellow crystals of **1-Eu**. Yield = 0.3537 g, 0.334 mmol, 43%. Anal calcd (%) for $C_{48}H_{108}O_3P_2Si_4Eu$: C, 54.41; H, 10.27. Found (%): C, 54.05; H, 10.22. ^{1}H NMR (400 MHz, d_6-benzene, 298 K): Data between +200 and –200 ppm could not be interpreted due to paramagnetic broadening. ^{13}C{^{1}H} NMR (101 MHz, d_6-benzene, 298 K): Not observed due to paramagnetic broadening. ^{29}Si DEPT90 NMR (79 MHz, d_6-benzene, 298 K): Not observed due to paramagnetic broadening. ^{31}P{^{1}H} NMR (162 MHz, d_6-benzene, 298 K): Not observed due to paramagnetic broadening. FTIR ν/cm^{-1}: 2941 (m), 2859 (s), 1463 (m), 1377 (w), 1225 (w), 1070 (w), 1007 (m), 989 (m), 873 (s).

[Yb{P(Si^{i}Pr$_3$)$_2$}$_2$(THF)$_2$] (1-Yb). Prepared by the same method as **1-Sm** using [$YbI_2(THF)_2$] (0.5711 g, 1 mmol) and [Na{P(Si^{i}Pr$_3$)$_2$}]$_n$ (1.1698 g, 2 mmol) to give yellow crystals of **1-Yb**. Yield = 0.4812 g, 0.477 mmol, 48%. Anal calcd (%) for $C_{44}H_{100}O_2P_2Si_4Yb$: C, 52.40; H, 9.99. Found (%): C, 50.65; H, 10.24. ^{1}H NMR (400 MHz, d_6-benzene, 298 K): δ 1.41 (br, 92H, C*H*(C*H*$_3$)$_2$, C*H*(C*H*$_3$)$_2$ and THF-C*H*$_2$), 3.85 (m, br, 8H, THF-C*H*$_2$). ^{13}C{^{1}H} NMR (101 MHz, d_6-benzene, 298 K): δ 16.90 (Vir.t, $^2J_{PC}$ = 10.3 Hz, *C*H(CH$_3$)$_2$), 20.57 (Vir.t, $^3J_{PC}$ = 3.6 Hz, CH(*C*H$_3$)$_2$), THF resonances not observed. ^{29}Si DEPT90 NMR (79 MHz, d_6-benzene, 298 K): δ 24.30, (Vir. t, $^1J_{PSi}$ = 15.8 Hz, (P*Si*). ^{31}P{^{1}H} NMR (162 MHz, d_6-benzene, 298 K): δ –301.10 (s, $^1J_{YbP}$ = 1382.1 Hz, $^1J_{PSi}$ = 18.1 Hz, Yb*P*). ^{171}Yb{^{1}H} NMR (71 MHz, d_6-benzene, 298 K): δ 682.0 (t, $^1J_{YbP}$ = 1382.9 Hz, *Yb*P). FTIR ν/cm^{-1}: 2947 (m), 2869 (s), 1469 (m), 1379 (w), 1235 (w), 1069 (w), 1011 (s), 873 (s).

Associated Content

Supporting Information

Additional experimental details, materials, methods, and data associated with this manuscript are compiled in the Supporting Information.

Additional Information

Research data files supporting this publication are available from FigShare at https://figshare.com/doi/ 10.6084/m9.figshare.26236493.

Accession Codes

2364164–2364167 contain the supplementary crystallographic data for this paper. These data can be obtained free of charge via https://www.ccdc.cam.ac.uk/structures/, or by emailing data_request@ccdc.cam.ac.uk, or by contacting The Cambridge Crystallographic Data Center, 12 Union Road, Cambridge, CB2 1EZ, UK; fax: +44 1223 336033.

Notes

The authors declare no competing financial interest.

Acknowledgements

We thank the European Research Council (CoG-816268) and the UK Engineering and Physical Sciences Research Council (EPSRC) (EP/P001386/1) for funding. We acknowledge the EPSRC UK National Electron Paramagnetic Resonance Service for access to the EPR facility and SQUID magnetometer (EP/S033181/1), and the NNUF EPSRC CRR facilities at the University of Manchester, supported by the National Nuclear User Facility, for emission spectroscopy (EP/T011289/1). We thank The University of Manchester for a Dame Kathleen Ollerenshaw Research Fellowship to M.S.O. We thank Prof. Deborah Kays and Dr Olivia Churchill for providing an improved synthesis of $[Na\{P(Si^{i}Pr_3)_2\}]_n$.[31]

Author Contributions

J. B. and D. P. M. conceptualized the idea. J. B. designed the synthetic conditions and performed the synthesis and standard characterization of all complexes. D. P. M. supervised the work. J. B. solved the crystallographic data for all complexes and G. W. collected and finalized the crystallographic data. A. B. and E. J. L. M collected and interpreted SQUID and EPR data. J. B. performed and interpreted *ab initio* calculations with supervision from M. S. O. L. N. collected and interpreted the luminescence data. J. B. wrote the first draft of the manuscript. J. B. compiled the Supplementary Information. D. P. M. revised the article for submission with input from all co-authors.

References

1. *The Lanthanides and Actinides*, Liddle, S. T.; Mills, D. P.; Natrajan, L. S. Eds. World Scientific Publishing Europe Ltd.: Singapore, 2022.

2. Mills, D. P.; Liddle, S. T. Ligand Design in Modern Lanthanide Chemistry, in *Ligand Design in Metal Chemistry: Reactivity and Catalysis*, Lundgren, R; Stradiotto, M. Eds. John Wiley and Sons Ltd.: Chichester, 2016.

3. Ortu, F.; Mills, D. P. Chapter 306. Low Coordinate Rare Earth and Actinide Complexes, in *Handbook on the Physics and Chemistry of Rare Earths*, Bünzli, J.-C. G.; Pecharsky, V. K. Eds. Elsevier B. V.: Amsterdam, 2019, **55**, 1.

4. *Lanthanides and Actinides in Molecular Magnetism*, Layfield, R. A.; Murugesu, M. Eds. Wiley-VCH: Berlin, 2015.

5. Rinehart, J. D.; Long, J. R. Exploiting single-ion anisotropy in the design of f-element single-molecule magnets. *Chem. Sci.* **2011**, *2*, 2078–2085.

6. *Luminescence of Lanthanide Ions in Coordination Compounds and Nanomaterials*, de Bettencourt-Dias, A. Ed. John Wiley and Sons Ltd.: Chichester, 2014.

7. *Optical Spectroscopy of Lanthanides: Magnetic and Hyperfine Interactions*, Wybourne, B. G.; Smentek, L. Eds. CRC Press: Boca Raton, 2007.

8. Bünzli, J.-C. G. Benefiting from the Unique Properties of Lanthanide Ions. *Acc. Chem. Res.* **2006**, *39*, 53–61.

9. Shibasaki, M.; Yoshikawa, N. Lanthanide Complexes in Multifunctional Asymmetric Catalysis. *Chem. Rev.* **2002**, *102*, 2187–2210.

10. Goodwin, C. A. P.; Mills, D. P. Silylamides: towards a half-century of stabilising remarkable f-element chemistry, in *Specialist Periodical Reports: Organometallic Chemistry: Vol. 41*, Fairlamb, I. J. S.; Lynam, J.; Patmore N. J.; Elliott, P. RSC Publishing: Cambridge, UK, 2017; pp. 123–156.

11. Roesky, P. W. Bulky Amido Ligands in Rare Earth Chemistry – Syntheses, Structures, and Catalysis. *Z. Anorg. Allg. Chem.* **2003**, *629*, 1881–1894.

12. *Metal Amide Chemistry*, Lappert, M; Protchenko, A; Power, P; Seeber, A. Eds. John Wiley and Sons Ltd.: Chichester, 2008.

13. Anwander, R. Lanthanide amides, in *Organolanthoid Chemistry: Synthesis, Structure, Catalysis*, Herrmann, W. A. Ed. Springer-Verlag: Berlin/Heidelberg, *Top. Curr. Chem.* **1996**, *179*, 33–112.

14. Du, J.; Cobb, P. J.; Ding, J.; Mills, D. P.; Liddle, S. T. f-Element heavy pnictogen chemistry. *Chem. Sci.* **2024**, *15*, 13–45.

15. Li, T.; Kaercher, S.; Roesky, P. W. Synthesis, structure and reactivity of rare-earth metal complexes containing anionic phosphorus ligands. *Chem. Soc. Rev.* **2014**, *43*, 42–57.

16. Giusti, L.; Landaeta, V. R.; Vanni, M.; Kelly, J. A.; Wolf, R.; Caporali, M. Coordination chemistry of elemental phosphorus. *Coord. Chem. Rev.* **2021**, *441*, 213927.

17. Bradley, D. C.; Ghotra, J. S.; Hart, F. A. Low co-ordination numbers in lanthanide and actinide compounds. Part I. The preparation and characterization of tris{bis(trimethylsilyl)-amido}lanthanides. *J. Chem. Soc., Dalton Trans.* **1973**, *10*, 1021–1023.

18. Bradley, D. C.; Ghotra, J. S.; Hart, F. A. Three-co-ordination in lanthanide chemistry: tris[bis(trimethylsilyl)amido]lanthanide(III) compounds. *J. Chem. Soc. Chem. Commun.* **1972**, *6*, 349–350.

19. Tilley, T. D.; Zalkin, A.; Andersen, R. A.; Templeton, D. H. Divalent lanthanide chemistry. Preparation of some four- and six-coordinate bis[(trimethylsilyl)amido] complexes of europium(II). Crystal structure of bis[bis(trimethylsilyl)amido]bis(1,2-dimethoxyethane)europium(II). *Inorg. Chem.* **1981**, *20*, 551–554.

20. Woen, D. H.; Chen, G. P.; Ziller, J. W.; Boyle, T. J.; Furche, F.; Evans, W. J. Solution Synthesis, Structure, and CO_2 Reduction Reactivity of a Scandium(II) Complex, $\{Sc[N(SiMe_3)_2]_3\}^-$. *Angew. Chem. Int. Ed.* **2017**, *56*, 2050–2053.

21. Chilton, N. F.; Goodwin, C. A. P.; Mills, D. P.; Winpenny, R. E. P. The first near-linear bis(amide) f-block complex: a blueprint for a high temperature single molecule magnet. *Chem. Commun.* **2015**, *51*, 101–103.

22. Goodwin, C. A. P.; Chilton, N. F.; Vettese, G. F.; Moreno Pineda, E.; Crowe, I. F.; Ziller, J. W.; Winpenny, R. E. P.; Evans, W. J.; Mills, D. P. Physicochemical Properties of Near-Linear Lanthanide(II) Bis(silylamide) Complexes (Ln = Sm, Eu, Tm, Yb). *Inorg. Chem.* **2016**, *55*, 10057–10067.

23. Baldwin, J.; Bonham, K. L.; Thompson, T. R. C.; Gransbury, G. K.; Whitehead, G. F. S.; Vitorica-Yrezabal, I. J.; Lee, D.; Chilton, N. F.; Mills, D. P. ^{31}P NMR chemical shift anisotropy in paramagnetic lanthanide phosphide complexes. *ChemRxiv* **2024**, *submitted*.

24. Baldwin, J.; Brookfield, A.; Whitehead, G. F. S.; Natrajan, L. S.; McInnes, E. J. L.; Oakley, M. S.; Mills, D. P. Isolation and electronic structures of lanthanide(II) bis(trimethylsilyl)phosphide complexes. *ChemRxiv* **2024**, DOI:10.26434/chemrxiv-2024-bl9lf.

25. Rabe, G. W.; Riede, J.; Schier, A. Structural Diversity in Lanthanide Phosphido Complexes. Formation and X-ray Crystal Structure Determination of an Unusual Dinuclear Phosphido Complex

of Divalent Samarium: $[(Me_3Si)_2P]Sm[\mu\text{-}P(SiMe_3)_2]_3Sm(thf)_3\cdot C_7H_8$. *Organometallics* **1996**, *15*, 439–441.

26. Emerson-King, J.; Gransbury, G. K.; Whitehead, G. F. S.; Vitorica-Yrezabal, I. J.; Rouzières, M.; Clérac, R.; Chilton, N. F.; Mills, D. P. Isolation of a Bent Dysprosium Bis(amide) Single-Molecule Magnet. *J. Am. Chem. Soc.* **2024**, *146*, 3331–3342.

27. Westerhausen, M.; Löw, R.; Schwarz, W. NMR-spektroskopische und strukturelle charakterisierung der tri-*iso*-propylsilylphosphanide des calciums. *J. Organomet. Chem.* **1996**, *513*, 213–229.

28. Westerhausen, M.; Rotter, T.; Görls, H.; Birg, C.; Warchhold, M.; Nöth, H. Lithium Bis(triisopropylsilyl)phosphanide and its Pentacarbonyltungsten Adduct: Synthesis and Crystal Structures of the Dimer $[(thf)Li\text{-}P(SiiPr_3)_2]_2$ and the Solvent-Separated Ion Pair $[(thf)_4Li]^+[(OC)_5W\text{-}P(SiiPr_3)_2]^-$. *Z. Naturforsch., B: Chem. Sci.* **2005**, *60*, 766–770.

29. Bauda, M.; Glinka, K. Lithium Dihydrogen Phosphide, in *Inorganic Syntheses Vol. 27*, Ginsberg, A. P. Ed. John Wiley and Sons Inc.: New York, 1990; pp 228-229.

30. Kosarev, S. A.; Collier, S. J. Tris(trimethylsilyl)phosphine, in *Encyclopedia of Reagents for Organic Synthesis*, John Wiley & Sons, Ltd: Chichester, 2011.

31. Churchill, O. P.; Dase, A.; Taylor, L. J.; Argent, S. P.; Coles, N. T.; Walker; G. S.; Kays, D. L. Synthesis of the bulky phosphanide $[P(Si^iPr_3)_2]^-$ and its stabilisation of low-coordinate Group 12 complexes. *ChemRxiv* **2024**, *submitted*.

32. Gabbaï, F. P.; Chirik, P. J.; Fogg, D. E.; Meyer, K.; Mindiola, D. J.; Schafer, L. L.; You, S.-L. An Editorial about Elemental Analysis. *Organometallics* **2016**, *35*, 3255–3256.

33. Fadeeva, V. P.; Tikhova, V. D.;Nikulicheva, O. N. Elemental analysis of organic compounds with the use of automated CHNS analyzers. *J. Anal. Chem.* **2008**, *63*, 1094–1106.

34. Nicholas, H. M.; Goodwin, C. A. P.; Kragskow, J. G. C.; Lockyer, S. J.; Mills, D. P. Structural Characterization of Lithium and Sodium Bulky Bis(silyl)amide Complexes. *Molecules* **2018**, *23*, 1138–1153.

35. Goodwin, C. A. P.; Réant, B. L. L.; Kragskow, J. G. C.; DiMucci, I. M.; Lancaster, K. M.; Mills, D. P.; Sproules, S. Heteroleptic samarium(III) halide complexes probed by fluorescence-detected L_3-edge X-ray absorption spectroscopy. *Dalton Trans*. **2018**, *47*, 10613–10625.

36. Shannon, R. D. Revised Effective Ionic Radii and Systematic Studies of Interatomic Distances in Halides and Chalcogenides. *Acta Cryst*allogr. *A* **1976**, *A32*, 751–767.

37. Addison, A. W.; Rao, T. N.; Reedijk, J.; van Rijn, J.; Verschoor, G. C. Synthesis, structure, and spectroscopic properties of copper(II) compounds containing nitrogen–sulphur donor ligands; the crystal and molecular structure of aqua[1,7-bis(*N*-methylbenzimidazol-2′-yl)-2,6-dithiaheptane]copper(II) perchlorate. *J. Chem. Soc*., *Dalton Trans.* **1984**, *7*, 1349–1356.

38. Alvarez, S.; Alemany, P.; Casanova, D.; Cirera, J.; Llunell, M.; Avnir, D. Shape maps and polyhedral interconversion paths in transition metal chemistry. *Coord*. *Chem*. *Rev*. **2005**, *249*, 1693–1708.

39. Yang, L.; Powell, D. R.; Houser, R. P. Structural variation in copper(i) complexes with pyridylmethylamide ligands: structural analysis with a new four-coordinate geometry index, τ_4. *Dalton Trans*. **2007**, *9*, 955–964.

40. Rabe, G. W.; Yap, G. P. A.; Rheingold, A. L. Divalent Lanthanide Chemistry: Three Synthetic Routes to Samarium(II) and Ytterbium(II) Bis(phosphido) Species Including the Structural Characterization of $Yb[PPh_2]_2(thf)_4$ and $Sm[PPh_2]_2(N\text{-}MeIm)_4$. *Inorg*. *Chem*. **1995**, *34*, 4521–4522.

41. Clegg, W.; Izod, K.; Liddle, S. T.; O’Shaughness, P.; Sheffield, J. M. A convenient route to lanthanide triiodide THF solvates. Crystal structures of $LnI_3(THF)_4$ [Ln = Pr] and $LnI_3(THF)_{3.5}$ [Ln = Nd, Gd, Y]. *Organometallics* **2000**, *19*, 2090–2096.

42. Groom, C. R.; Bruno, I. J.; Lightfoot, M. P.; Ward, S. C. The Cambridge Structural Database. *Acta. Crystallogr. B* **2016**, *72*, 171–179.

43. Westerhausen, M.; Hartmann, M.; Schwarz, W. Syntheses and structure of dimeric yttrium tris [bis(trimethylsilyl)phosphanide]; X-ray structures of $[(thf)LiCl\cdot(thf)_2LiP^tBu_2]_2$ and $Y[CH(SiMe_3)_2]_3$. *Inorg. Chim. Acta*. **1998**, *269*, 91–100.

44. Yatabe, T.; Karasawa, M.; Isobe, K.; Ogo, S.; Nakai, H. A naphthyl-substituted pentamethylcyclopentadienyl ligand and its Sm(ii) bent-metallocene complexes with solvent-induced structure change. *Dalton Trans.* **2012**, *41*, 354–356.

45. Maria, L.; Soares, M.; Santos, I. C.; Sousa, V. R.; Mora, E.; Marçalo J.; Luzyanin, K. V. A novel samarium(ii) complex bearing a dianionic bis(phenolate) cyclam ligand: synthesis, structure and electron-transfer reactions. *Dalton Trans*. **2016**, *45*, 3778–3790.

46. Prasad, E.; Knettle, B. W.; Flowers, R. A. Investigation of the $[Sm\{N(SiMe_3)_2\}_2]$ Reducing System in THF. Rate and Mechanistic Studies. *J. Am. Chem. Soc.* **2002**, *124*, 14663–14667.

47. Rabe, G. W; Riede, J.; Schier, A. Synthesis, X-ray Crystal Structure Determination, and NMR Spectroscopic Investigation of Two Homoleptic Four-Coordinate Lanthanide Complexes: Trivalent $(^tBu_2P)_2La[(\mu\text{-}P^tBu_2)_2Li(thf)]$ and Divalent $Yb[(\mu\text{-}P^tBu_2)_2Li(thf)]_2$. *Inorg. Chem.* **1996**, *35*, 40–45.

48. Bünzli, J.-C. G.; Eliseeva, S. V. Basics of Lanthanide Photophysics, in *Lanthanide Luminescence Photophysical, Analytical and Biological Aspects*, P. Hänninen P.; Härmä, H. Eds. Springer-Verlag: Berlin/Heidelberg, 2010.

49. Kuda-Wedagedara, A. N. W.; Wang, C.; Martin, P. D.; Allen, M. J. Aqueous Eu^{II}-Containing Complex with Bright Yellow Luminescence. *J. Am. Chem. Soc.* **2015**, *137*, 4960–4963.

50. Dorenbos, P. Anomalous luminescence of Eu^{2+} and Yb^{2+} in inorganic compounds. *J. Phys.: Condens. Matter*. **2003**, *15*, 2645–2665.

51. Goodwin, C. A. P.; Chilton, N. F.; Natrajan, L. S.; Boulon, M-E.; Ziller, J. W.; Evans, W. J.; Mills, D. P. Investigation into the Effects of a Trigonal-Planar Ligand Field on the Electronic

Properties of Lanthanide(II) Tris(silylamide) Complexes (Ln = Sm, Eu, Tm, Yb). *Inorg*. *Chem*. **2017**, *56*, 5959–5970.

52. Jenks, T. C.; Allen, M. J. Divalent Lanthanide Luminescence in Solution, in *Modern Applications of Lanthanide Luminescence*, de Bettencourt-Dias, A. Ed. Springer: Switzerland, 2021.

53. Garcia, J.; Allen, M. J. Developments in the Coordination Chemistry of Europium(II). *Chem*. *Eur*. *J*. **2012**, *29*, 4550–4563.

54. Starynowicz, P.; Bukietyńska, K. A Europium(II) Complex with Benzo-15-Crown-5. *Chem*. *Eur*. *J*. **2002**, *7*, 1835–1838.

55. Shinoda, S.; Nishioka, M.; Tsukube, H. *In situ* generation of fluorescent macrocyclic europium(II) complexes via zinc reduction. *J*. *Alloys Compd*. **2009**, *2*, 603–605.

56. Englman, R.; Jortner, The energy gap law for radiationless transitions in large molecules. J. *Mol*. *Phys*. **1970**, *2*, 145–164.

57. Nodaraki, L. E.; Liu, J.; Ariciu, A-M.; Ortu, F.; Oakley, M. S.; Birnoschi, L.; Gransbury, G. K.; Cobb, P. J.; Emerson-King, J.; Chilton, N. F.; Mills, D. P.; McInnes, E. J. L.; Tuna, F. Metal–carbon bonding in early lanthanide substituted cyclopentadienyl complexes probed by pulsed EPR spectroscopy. *Chem*. *Sci*. **2024**, *15*, 3003–3010.

58. Stoll, S.; Schweiger, A. EasySpin, a comprehensive software package for spectral simulation and analysis in EPR. *J. Magn. Reson.* **2006**, *178,* 42–55.

59. Adamo. C.; Barone, V. Toward reliable density functional methods without adjustable parameters: The PBE0 model. *J. Chem. Phys.* **1999**, *110*, 6158–6169.

60. Galván, I. F.; Vacher, M.; Alavi, A.; Angeli, C.; Aquilante, F.; Autschbach, J.; Bao, J. J.; Bokarev, S. I.; Bogdanov, N. A.; Carlson, R. K.; L. F. Chibotaru, L. F.; Creutzberg, J.; Dattani, N.; Delcey, M. G.; Dong, S. S.; Dreuw, A.; Freitag, L.; Frutos, L. M.; Gagliardi, L.; Gendron, F.; Giussani, A.; Gonzàlez, L.; Grell, G.; Guo, M.; Hoyer, C. E.; Johansson, M.; Keller, S.; Knecht, S.; Kovačević, G.; Källman, E.; Manni, G. L.; Lundberg, M.; Ma, Y.; Mai, S.; Malhado, J. P.;

Malmqvist, P. Å.; Marquetand, P.; Mewes, S. A.; Norell, J.; Olivucci, M.; Oppel, M.; Phung, Q. M.; Pierloot, K.; Plasser, F.; Reiher, M.; Sand, A. M.; Schapiro, I.; Sharma, P.; Stein, C. J.; Sørensen, L. K.; Truhlar, D. G.; Ugandi, M.; Ungur, L.; Valentini, A.; Vancoillie, S.; Veryazov, V.; Weser, O.; Wesolowski, T. A.; Widmark, P.-O.; Wouters, S.; Zech, A.; Zobel, J. P.; Lindh, R. OpenMolcas: From Source Code to Insight. *J. Chem. Theory Comput.* **2019**, *15*, 5925–5964.

61. Girard, P.; Namy, J. L.; Kagan, H. B. Divalent lanthanide derivatives in organic synthesis. 1. Mild preparation of samarium iodide and ytterbium iodide and their use as reducing or coupling agents. *J. Am. Chem. Soc.* **1980**, *8*, 2693–2698.

62. *CrysAlis PRO*, Agilent Technologies Ltd. Yarnton, England, 2014.

63. Sheldrick, G. M. Crystal structure refinement with *SHELXL*. *Acta Crystallogr. C* **2015**, *71*, 3–8.

64. Beck, T.; Krasauskas, A.; Gruene, T.; Sheldrick, G. M. A magic triangle for experimental phasing of macromolecules. *Acta Crystallogr. D* **2008**, *64*, 1179–1182.

65. Dolomanov, O. V.; Bourhis, L. J.; Gildea, R. J.; Howard, J. A. K.; Puschmann, H. *OLEX2*: a complete structure solution, refinement and analysis program. *J. Appl. Crystallogr.* **2009**, *42*, 339–341.

66. Farrugia, L. J. WinGX and ORTEP for Windows: an update. *J. Appl. Crystallogr.* **2012**, *45*, 849–854.

67. *Persistence of Vision Raytracer*, v.3.7, Persitance of Vision Raytracer Pty. Ltd., 2013.

68. Roos, B. O.; Lindh, R.; Malmqvist, P. Å.; Veryazov, V.; Widmark, P.-O. Main Group Atoms and Dimers Studied with a New Relativistic ANO Basis Set. *J. Phys. Chem. A* **2004**, *108*, 15, 2851–2858.

69. Roos, B. O.; Lindh, R.; Malmqvist, P. Å.; Veryazov, V.; Widmark, P.-O; Borin, A. C. New Relativistic Atomic Natural Orbital Basis Sets for Lanthanide Atoms with Applications to the Ce Diatom and LuF_3. *J. Phys. Chem. A* **2008**, *112*, 45, 11431–11435.

70. Aquilante, F.; Lindh, R.; Pedersen, T. B. Inner projection techniques for the low-cost handling of two-electron integrals in quantum chemistry. *J. Chem. Phys.* **2007**, *127*, 114107–114114.

71. Chibotaru, L. F.; Ungur, L. Ab initio calculation of anisotropic magnetic properties of complexes. I. Unique definition of pseudospin Hamiltonians and their derivation. *J. Chem. Phys.* **2012**, *137*, 6, 064112.

72. *Diamond-Crystal and Molecular Structure Visualization*; Crystal Impact v.4.6.8. Putz, H.; Brandenburg, K., Bonn, Germany, 2022.

73. Dolg, M.; Stoll, H.; Preuss, H. Energy-adjusted ab initio pseudopotentials for the rare earth elements. *J. Chem. Phys.* **1989**, *90*, 1730–1734.

74. Dunning, Jr., H., T. Gaussian basis sets for use in correlated molecular calculations. I. The atoms boron through neon and hydrogen. *J. Chem. Phys.* **1989**, *90*, 1007–1023.

75. Grimme, S.; Antony, J.; Ehrlich, S.; Krieg, H. A consistent and accurate *ab initio* parametrization of density functional dispersion correction (DFT-D) for the 94 elements H-Pu. *J. Chem. Phys.* **2010**, *132*, 154104.

76. *Gaussian 16, Revision C.01*, Frisch, M. J.; Trucks, G. W.; Schlegel, H. B.; Scuseria, G. E.; Robb, M. A.; Cheeseman, J. R.; Scalmani, G.; Barone, V.; Petersson, G. A.; Nakatsuji, H.; Li, X.; Caricato, M.; Marenich, A. V.; Bloino, J.; Janesko, B. G.; Gomperts, R.; Mennucci, B.; Hratchian, H. P.; Ortiz, J. V.; Izmaylov, A. F.; Sonnenberg, J. L.; Williams-Young, D.; Ding, F.; Lipparini, F.; Egidi, F.; Goings, J.; Peng, B.; Petrone, A.; Henderson, T.; Ranasinghe, D.; Zakrzewski, V. G.; Gao, J.; Rega, N.; Zheng, G.; Liang, W.; Hada, M.; Ehara, M.; Toyota, K.; Fukuda, R.; Hasegawa, J.; Ishida, M.; Nakajima, T.; Honda, Y.; Kitao, O.; Nakai, H.; Vreven, T.; Throssell, K.; Montgomery, Jr., J. A.; Peralta, J. E.; Ogliaro, F.; Bearpark, M. J.; Heyd, J. J.; Brothers, E. N.; Kudin, K. N.; Staroverov, V. N.; Keith, T. A.; Kobayashi, R.; Normand, J.; Raghavachari, K.; Rendell, A. P.; Burant, J. C.; Ivengar, S. S.; Tomasi, J.; Cossi, M.; Millam, J. M.; Klene, M.; Adamo, C.; Cammi, R.; Ochterski, J. W.; Martin, R. L.; Morokuma, K.; Farkas, O.; Foresman, J. B.; Fox, D. J. Gaussian, Inc., Wallingford CT, 2016.

77. Lu, T.; Chen, F. Multiwfn: A Multifunctional Wavefunction Analyzer. *J. Comput. Chem.* **2012**, *33*, 580–592.